metals

MDPI

Article

Exploring Resistance Spot Welding for Grade 2 Titanium Alloy: Experimental Investigation and Artificial Neural Network Modeling

Marwan T. Mezher [1,2], Diego Carou [1,*] and Alejandro Pereira [1]

[1] Departamento de Deseño na Enxeñaría, Universidade de Vigo, 36310 Vigo, Spain; marwantahir90@gmail.com (M.T.M.); apereira@uvigo.gal (A.P.)
[2] Institute of Applied Arts, Middle Technical University, Baghdad 10074, Iraq
* Correspondence: diecapor@uvigo.gal

Abstract: The resistance spot welding (RSW) process is still widely used to weld panels and bodies, particularly in the automotive, railroad, and aerospace industries. The purpose of this research is to examine how RSW factors such as welding current, welding pressure, welding time, holding time, squeezing time, and pulse welding affect the shear force, micro-hardness, and failure mode of spot welded titanium sheets (grade 2). Resistance spot welded joints of titanium sheets with similar and dissimilar thicknesses of 1–1 mm, 0.5–0.5 mm, and 1–0.5 mm were evaluated. The experimental conditions were arranged using the design of experiments (DOE). Moreover, artificial neural network (ANN) models were used. Different training and transfer functions were tested using the feed-forward backpropagation approach to find the optimal ANN model. According to the experimental results, the maximum shear force was 5.106, 4.234, and 4.421 kN for the 1–1, 0.5–0.5, and 1–0.5 mm cases, respectively. The hardness measurements showed noticeable improvement for the welded joints compared to the base metal. The findings revealed that the 0.5–0.5 mm case gives the highest nugget and heat-affected zone (HAZ) hardness compared to other cases. Moreover, different failure modes like pull-out nugget, interfacial, and partial failure between the pull-out nugget and interfacial failure were noticed. The ANN outcomes based on the mean squared error (MSE) and coefficient of determination (R^2) as validation metrics demonstrated that using the Levenberg–Marquardt (Trainlm) training function with the log sigmoid transfer function (Logsig) gives the best prediction, where R^2 and MSE values were 0.98433 and 0.01821, respectively.

Keywords: resistance spot welding; titanium sheet; artificial neural network; shear force; micro-hardness; unequal thicknesses

Citation: Mezher, M.T.; Carou, D.; Pereira, A. Exploring Resistance Spot Welding for Grade 2 Titanium Alloy: Experimental Investigation and Artificial Neural Network Modeling. *Metals* **2024**, *14*, 308. https://doi.org/10.3390/met14030308

Academic Editor: Jean-Michel Bergheau

Received: 21 January 2024
Revised: 4 March 2024
Accepted: 4 March 2024
Published: 6 March 2024

1. Introduction

Resistance spot welding (RSW), which is categorized as a pressure welding technique, is now the primary assembly process used in the automobile industry and other sectors. For several decades, the aerospace industry has recognized the economic benefits of spot welding [1–4]. Around 90% of all vehicle body assemblies use resistance spot welds [5]. For example, an average automobile includes more than three thousand spot welds [6]. In the case of bus and coach bodies, this figure may rise to as many as 8000 spots. Spot welds provide several benefits over other types of welding [7–9], including a shorter welding time, the elimination of the need for filler material, and improved dimensional accuracy.

Titanium and its alloys have unique mechanical and physical properties and find applications in industrial fields [10] such as aviation, medical industry, and chemical engineering due to their low density and high strength [11]. Titanium alloys have been welded using a variety of welding processes, including tungsten inert gas welding (TIG), even though TIG creates a weld structure that is coarse and induces an abundance of welding residual stress and distortion [12,13].

Laser and electron beam welding are considered superior alternatives to TIG welding because of their advantages, such as high welding speed and minimal welding distortion. However, laser welding and electron beam welding are better suited for butt joints than lap joints due to their high depth-to-width ratio penetration capabilities [12,13]. Moreover, investment and operating costs are high [12–15]. Even though brazing is straightforward to apply, welding titanium alloys often takes a long time due to the vacuum conditions necessary and high temperatures [14,15].

The novel welding process of friction stir welding has been used to weld thin sheets for butt and lap joints for the past 30 years. However, some drawbacks, such as the high melting point of titanium alloys and the contact pressure of the metal sheets with the friction tool, must be considered [16–18].

Zhang et al. [19] examined the RSW of Ti6Al4V alloy sheets (Rickard Specialty Metals, Ontario, CA, USA), analyzing weld nugget formation, mechanical properties, and microstructure. Electrode force dominates weld nugget width, although welding current and time also matter. El Kandaoui et al. [20] studied butt-jointed Ti-6Al-4V alloys (5125 and 5326) using fiber laser welding. The analysis of the microstructure of the base material revealed a coarse $\alpha + \beta$ microstructure in the 5125 grade and a thinner microstructure with small α grains and β particles at grain boundaries in the 5326 grade. Chen et al. [21] created a precise online monitoring system for resistance spot welded joints of TB2 titanium alloy to assess joint quality by collecting data about electrode pressure, welding voltage, welding current, and electrode displacement.

Online inspection verified the presence of splashes and imperfect welding fusion. Fatmahardi et al. [6] found that the fractured surface of RSW for Ti-6Al-4V was cup-and-cone pull-out failure, proving that the weld nugget is stronger than the heat-affected zone (HAZ) and base metal. Dissimilar micro-RSW of austenitic stainless steel 316L and Ti-6Al-4V titanium alloy was studied by Mansor et al. [22]. The tensile shear test showed that the highest shear force for all welded specimens was 378.25 N and that all of them failed in an interfacial failure (IF) mode. Li et al. [23] found that welding current considerably affects joint tensile shear properties, whereas welding time and electrode force had minor effects on the RSW of commercial titanium and AA 6061-T6 Aluminum alloy (Textron Steel and Alloys, Mumbai, India).

Using load capacity tests, Lacki et al. [24] evaluated the RSW composite beam made of titanium alloy grades 5 and 2. Two samples failed at joints with two parallel shear welds. Another study by Anna et al. [25] evaluated the titanium grade 5 beam using RSW. Joint strength improved with high welding current and short welding time, with the greatest results at 37 A and 15 ms, respectively.

Based on neural network (NN) observations, Arunchai et al. [26] estimated weld quality using ANN for RSW. The model predictions were 95% accurate. Weld quality and failure stress of titanium resistance spot welded joints were estimated by Wan et al. [27] using backpropagation and probabilistic neural network models. The backpropagation NN model effectively estimated failure load, whereas the probabilistic neural method accurately estimated weld quality. Ghafarallahi et al. [28] used the finite element method (FEM) and multilayer perceptron (MLP) neural network model findings to categorize the spot weld diameter. They noted that the ANN predicts weld diameter better than FEM.

The first comprehensive examination of titanium-resistant butt spot joints was by Bi et al. [29]. Fracture modes at interfaces affect the component microstructure and joint quality.

Piotr and Judyta [30] explored the hardness and load capacity of grade 2 and 5 titanium alloys. The results demonstrated that the hardness and resulting load are influenced by the arrangement of the grades, regardless of whether they are like grade 5 or different from grade 2. Yu et al. [31] used ultrasonic seam-assisted resistance spot welding (USRSW) to weld grade 4 titanium alloy and Q235 mild steel with a copper alloy interlayer. The findings were compared to traditional resistance spot welding (TRSW) with and without an interlayer. USRSW-Cu created an irregular weld, whereas TRSW produced a flat nugget.

The weld nugget is less prone to fracture because of its inhomogeneity. In addition, ultrasonic seam-assisted resistance spot welding with a copper interlayer (USRSW-Cu) generated 2.68 times the shear force of TRSW.

Using upset butt welding, Santhakumari et al. [32] joined AISI 304 with commercial titanium. The findings show that brittle intermetallic phases induce poor welded joint elongation. Preheating Ti-2Al-1Mn alloy (Western Alloys, Canning Vale, Australia) resistance spot welded joints was studied by Butsykin et al. [33]. Heating the nuggets reduced dispersion by 160%, increased fracture energy by 48%, and the maximum force by 15%. Niu et al. [34] welded Ti and Al alloys by resistance rivet welding. The findings indicate that solid Al and α2-AlTi3 solutions are the main contributors causing hardness enhancement.

A monel interlayer allowed Bi et al. [35] to produce brittle Ti-Fe intermetallic compounds (IMCs). IMCs form between titanium alloy and stainless steel RSW joints. Eliminating brittle IMCs greatly improved joint quality. Liu et al. [36] studied how porosity influenced TC17 titanium alloy welded joint fatigue at both ambient and high temperatures. The S-N curves of the welded joints were bilinear at 400 °C but single-linear at ambient temperature. Welded pores caused fatigue failure; however, temperature did not affect it. Mezher et al. [37] performed a finite element study on RSW of AISI 316L using ANSYS software 2020 R1. Adding the thermal contact resistance modification to the FE model improves temperature distribution prediction, as they confirmed.

According to the literature review, no prior research has comprehensively analyzed the effect of RSW parameters, particularly, the effect of welding current, welding, holding and squeeze times, pulse welding, and electrode welding pressure, on outputs such as the shear force, micro-hardness, and failure of the resultant joint. This lack of analysis specifically pertains to the RSW process of titanium alloy grade 2 with 0.5 and 1 mm thicknesses. Therefore, this research is presented, highlighting as a novelty the use of different neural network models built using various training and transfer functions to examine the RSW parameters on predicted shear compared to experimental results.

2. Materials and Methods

2.1. Materials and Specimens' Preparation

Titanium alloy (grade 2) sheets with thicknesses of 0.5 and 1 mm were used in the RSW process (Baoji Sunrise Dongsheng Industry & Trade Co., Ltd., Baoji, China). The dimensions of each sample were measured using the lap joint arrangement following the specifications of the AWS [38] as shown in Table 1. Table 2 lists the mechanical parameters of titanium alloy grade 2 and Table 3 summarizes its chemical composition.

Table 1. Dimensions of the RSW specimens.

Thickness (mm)	Length (mm)	Width (mm)	Overlap Region (mm)
0.5	76	16	16
1	100	25	25

Table 2. Mechanical properties of grade 2 titanium alloy.

Property	Tensile Strength (MPa)	Yield Strength (MPa)	Poisson's Ratio	Young Modulus (GPa)	Elongation (%)
Standard	≥400	275–450	0.37	105–120	≥25
Measured	428	318	0.37	113	28

Table 3. Chemical composition of grade 2 titanium alloy.

Element wt.%	Fe	O	N	C	H	Ti
Standard	≤0.3	≤0.25	≤0.03	≤0.08	≤0.015	Balance
Measured	0.062	0.11	0.0067	0.0055	0.001	Balance

Figure 1 depicts the schematic illustration of the test sample, and the dimensions are presented in Table 1. All titanium alloy grade 2 samples were mechanically polished with No. 800 grit abrasive paper to remove cutting edge burr, surface contaminants, and the oxide layer that had developed before being subjected to the RSW process. Ethanol was then used to clean the surface and eliminate any remaining contaminants. Taking this action is crucial in RSW to avoid the presence of expulsion welds that occur at random if the surface is contaminated.

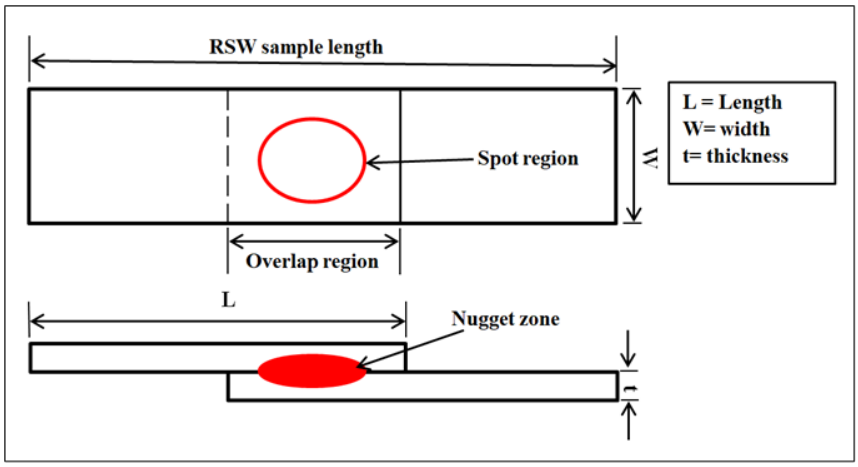

Figure 1. Schematic illustration of the RSW specimen.

2.2. Resistance Spot Welding Process

The RWMA group A class 2 type B chromium-zirconium-copper alloy dome-shaped electrode with a 4 mm circular contacting area was employed. The pressure was generated using a pneumatic system. The digital screen of the RSW machine was utilized to adjust the process parameters, including welding current, welding, squeeze, and holding times, and pulse welding. The experiments were carried out at standard laboratory room temperature. Welding parameters included a welding current range of 5000–7000 A, a welding time range of 0.6–1.4 s, a squeezing time range of 0.6–1.4 s, a holding time range of 0.5–1.5 s, a pulse welding range of 1–5, and a pressure range of 2–8 bar. To ensure that the electrode tip was properly positioned in the middle of the overlap region during welding, an X was marked on the top face center of the samples before welding started. Figure 2 shows a simplified diagram of the experimental welding equipment.

The experiments were arranged using the Design of Experiment (DOE) according to the Taguchi method using Minitab software 18, as detailed in Table 4. Figure 3 shows the resistance spot welded samples of the three cases. The RSW parameters used in the current work are described as follows:

Welding time: the duration applied to weld the samples.
Welding current: the amount of current provided by the source.
Pressure: the pressure exerted to hold the materials together during welding.
Squeeze time: the duration between the application of pressure and the welding process.
Hold time: the duration for which the pressure is maintained after the welding is completed.
Pulse welding: the alternating modulation of amperage between high and low points.

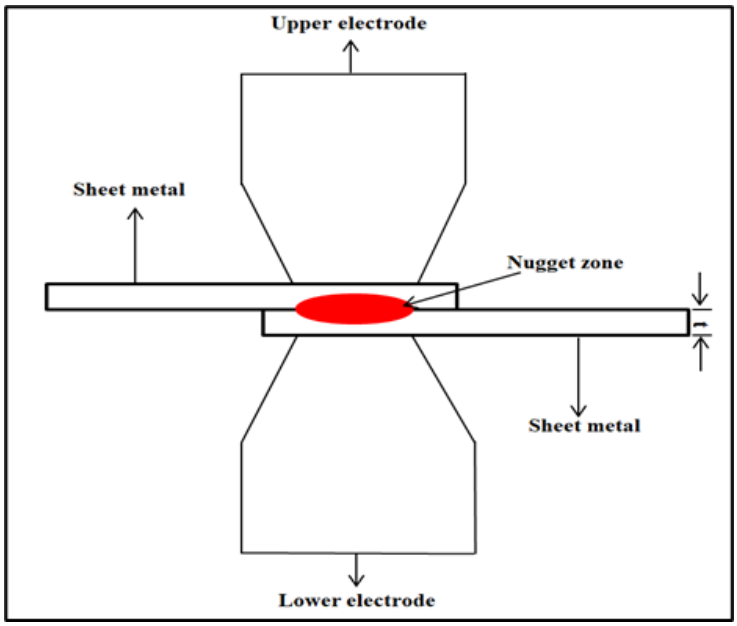

Figure 2. Schematic illustration of RSW process.

Table 4. RSW Experimental parameters according to the design of experiment (DOE). - means unitless.

No.	Welding Cases			Welding Current (A)	Pressure (bar)	Welding Time (s)	Squeeze Time (s)	Holding Time (s)	Pulse Welding (-)
1	A1	B1	C1	5000	2.0	0.6	0.6	0.50	1
2	A2	B2	C2	5000	3.5	0.8	0.8	0.75	2
3	A3	B3	C3	5000	5.0	1.0	1.0	1.00	3
4	A4	B4	C4	5000	6.5	1.2	1.2	1.25	4
5	A5	B5	C5	5000	8.0	1.4	1.4	1.50	5
6	A6	B6	C6	5500	2.0	0.8	1.0	1.25	5
7	A7	B7	C7	5500	3.5	1.0	1.2	1.50	1
8	A8	B8	C8	5500	5.0	1.2	1.4	0.50	2
9	A9	B9	C9	5500	6.5	1.4	0.6	0.75	3
10	A10	B10	C10	5500	8.0	0.6	0.8	1.00	4
11	A11	B11	C11	6000	2.0	1.0	1.4	0.75	4
12	A12	B12	C12	6000	3.5	1.2	0.6	1.00	5
13	A13	B13	C13	6000	5.0	1.4	0.8	1.25	1
14	A14	B14	C14	6000	6.5	0.6	1.0	1.50	2
15	A15	B15	C15	6000	8.0	0.8	1.2	0.50	3
16	A16	B16	C16	6500	2.0	1.2	0.8	1.50	3
17	A17	B17	C17	6500	3.5	1.4	1.0	0.50	4
18	A18	B18	C18	6500	5.0	0.6	1.2	0.75	5
19	A19	B19	C19	6500	6.5	0.8	1.4	1.00	1
20	A20	B20	C20	6500	8.0	1.0	0.6	1.25	2
21	A21	B21	C21	7000	2.0	1.4	1.2	1.00	2
22	A22	B22	C22	7000	3.5	0.6	1.4	1.25	3
23	A23	B23	C23	7000	5.0	0.8	0.6	1.50	4
24	A24	B24	C24	7000	6.5	1.0	0.8	0.50	5
25	A25	B25	C25	7000	8.0	1.2	1.0	0.75	1

Where: Case A (titanium alloy with a similar thickness of 1 mm), Case B (titanium alloy with a similar thickness of 0.5 mm), Case C (titanium alloy with dissimilar thicknesses of 1 and 0.5 mm).

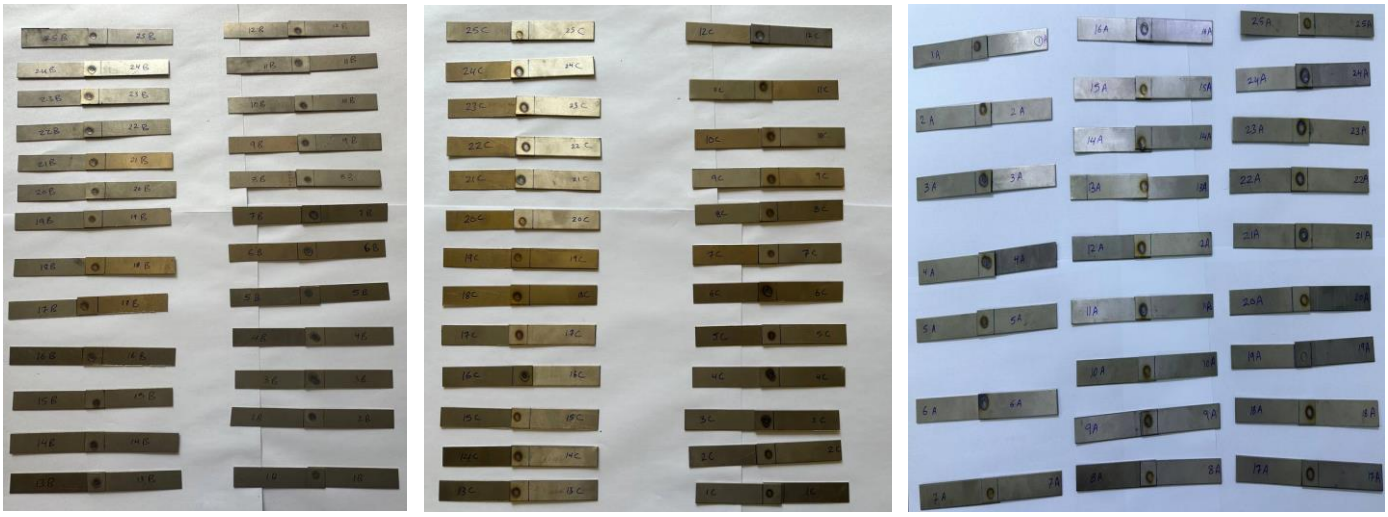

Figure 3. Resistance spot welded specimens, **Left**: Case B, **Centre**: Case C, **Right**: Case A.

2.3. Tensile Shear Test

The tensile shear test was conducted on the resistance spot welded joints to evaluate weld quality and determine the maximum shear force needed to break them. The tests were performed using a Universal Testing Machine with 50 kN maximum load and 5 mm/min of crosshead speed at room temperature, as depicted in Figure 4.

Figure 4. Tensile shear test of the RSW joints.

The results ascertained whether the welded connection failed due to a pull-out or an interfacial failure. The load-displacement curve was utilized to determine the optimum shear force. Furthermore, a fracture surface analysis was carried out to determine the failure mechanism of the shear test specimens. Optical microscope micrographs of the cracked specimen cross-section aided in evaluating the failure mechanism. Figure 5 shows the resistance spot welded samples of the three cases after undergoing a tensile shear test.

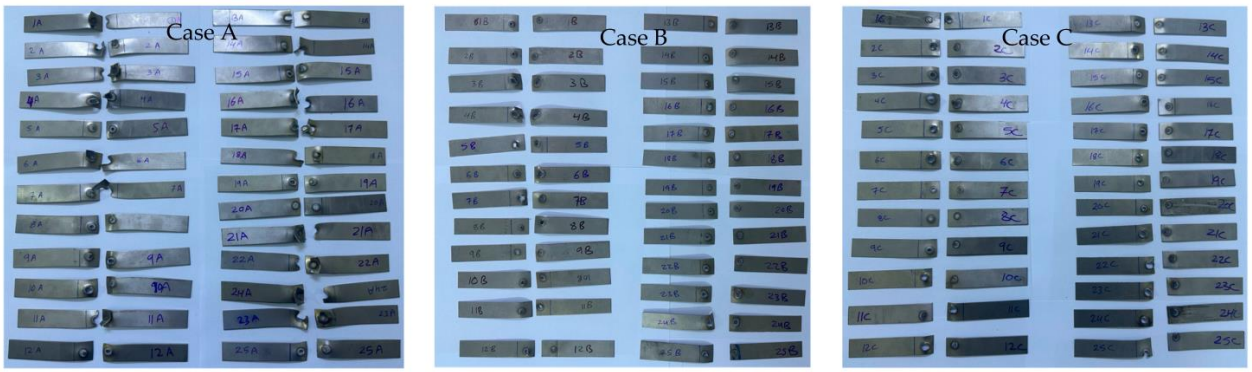

Figure 5. Fractured resistance spot welded specimens.

2.4. Micro-Hardness Measurements

The micro-hardness of the welds was determined by performing a Vickers test, employing a 2.98 N load and a 10 s dwell period, utilizing a pyramidal diamond indenter micro-hardness tester (HVS-1000 series, Laryee Testing Machines, Laryee Technology Co., Ltd., Beijing, China). Hardness tests were conducted at a consistent interval of 0.5 mm from each sample along a diagonal path originating from the base metal. This path traversed through the heat-affected zone and weld nugget zone, continuing through the other heat-affected zone, and ultimately reaching the base metal on the opposite side, as illustrated in Figure 6.

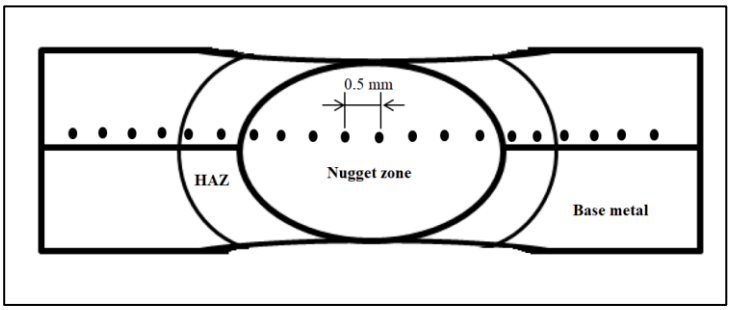

Figure 6. Micro-hardness positions along the weld profile.

Metallographic specimens were prepared by cutting the RSW welded joint through the center of the weld nugget perpendicular to the weld surface plane. As shown in Figure 7, the specimen was mounted in acrylic (a mixture of resin and hardener), followed by grinding and polishing in sequence to observe the microstructure and fracture morphology of the failed sample. Etching was performed at room temperature using a solution of 1% HCL, 1.5% HF, 2.5% HNO_3, and 95% distilled water, following the polishing procedure. An optical microscope was used to examine the morphology of the fractured specimens.

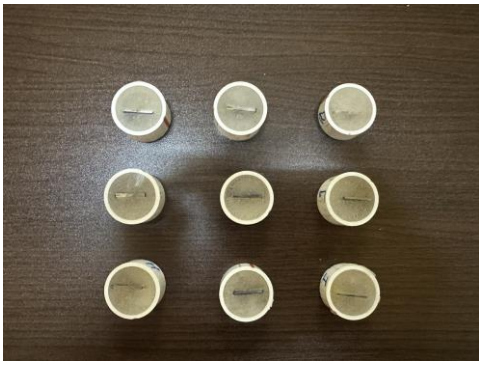

Figure 7. Mounted samples of microstructure and micro-hardness tests.

3. Artificial Neural Network (ANN)

The neural network model developed by McCulloch and Pitts study in the 1940s is identified as the earliest modern neural network model. Neural networks serve as valuable tools for constructing both linear and nonlinear models of complex tasks. The architecture of the ANNs closely mirrors the workings of the biological brain. The network structure is composed of a group of interconnected elements called neurons that process information delivered to the input of the network based on the principle of parallel processing. The ANN structure consists of the input and output layers. In addition, there is a hidden layer that separates the input and output layers. Each neural network contains many neurons, and the output neuron number is equivalent to the input variable. Transferring the weights forward and backward is generated according to the transfer and activation functions used in the layers of neurons [39]. A feed-forward backpropagation (BP) network was used in the current work to model an artificial neural network with a multilayer perceptron (MLP). The MLP equation is given below:

$$y = f(net) = \left(\sum_{i=1}^{n} w_i x + b\right)$$

where:

y: the outputs,
f: the activation function,
x: the input,
w_i: the weights,
b: the bias.

Neural network modelling was carried out using MATLAB R2021a. In ANN models, the input layer data were welding current, pressure, welding time, squeeze time, holding time, and pulse welding, whereas the tensile shear force was set as an output layer data. Moreover, the hidden layer number was 10.

Three different transfer functions with five training functions were used. The training functions were Levenberg–Marquardt (Trainlm), scaled conjugate gradient (Trainscg), conjugate gradient with Fletcher–Reeves updates (Traincgf), conjugate gradient with Powell-Beale restarts (Traincgb), and conjugate gradient with Polak–Ribiere updates (Traincgp). For each training function, three different transfer functions were individually employed at the hidden layer. The transfer functions were log sigmoid transfer (Logsig), hyperbolic tangent sigmoid (Tansig), and pure linear (Purelin). The hyperbolic tangent sigmoid (Tansig) was applied as the output layer's transfer function for all experiments.

Concerning the data distribution, 70% was used for training, 15% for testing, and 15% for validation [40]. Thus, 53 samples were used for training, 11 for testing, and 11 for validation. For the training parameters, the learning rate was 0.01, the goal was 0.001, and the epoch number was 1000. The accuracy of the neural network models was assessed based on the mean square error (MSE) and coefficient of determination (R^2). The validation criteria for predicting the output depend on minimizing the error between the actual and predicted data. Since the coefficient of determination (R^2) approached 1 and the mean square error was close to 0, the model indicated good performance in predicting data. Figure 8 shows the neural network structure.

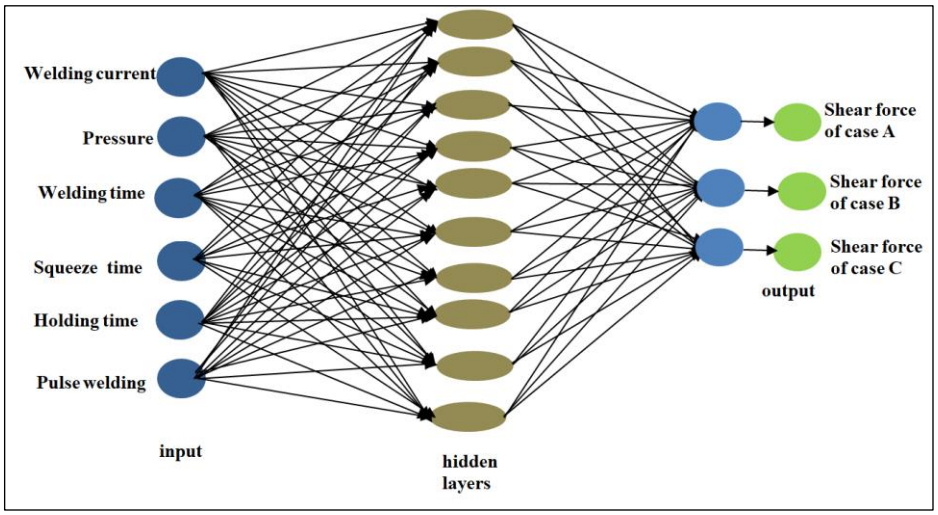

Figure 8. Neural network structure of the RSW process.

4. Results and Discussions

4.1. Tensile Shear Force

A series of 25 tensile shear tests were conducted for each case of 1–1 mm, 0.5–0.5 mm, and 0.5–1 mm for titanium alloy grade 2, as presented in Table 4. The objective of these experiments was to determine the appropriate RSW parameters that meet acceptable standards. The results proved that the RSW parameters have a direct influence on the tensile shear force of the welded joints.

Based on a design of experiments (DOE) study, the parameters for producing the strongest resistance spot joint in case A were welding current of 7000 A, welding time of 1 s, pressure of 6.5 bar, squeezing time of 0.8 s, holding time of 0.5 s, and pulse welding of 5. Under these conditions, the maximum shear force was 5.106 kN. Experiment 14 had the lowest shear force at 3.861 kN with a welding current of 6000 A, pressure of 6.5 bar, welding time of 0.6 s, squeezing time of 1 s, holding time of 1.5 s, and pulse welding of 2 as shown in Table 5.

Table 5. Shear force results for the three RSW cases.

No.	Case A	Shear Force (kN)	Case B	Shear Force (kN)	Case C	Shear Force (kN)
1	A1	4.423	B1	2.422	C1	3.665
2	A2	4.052	B2	2.317	C2	3.916
3	A3	4.918	B3	3.352	C3	3.412
4	A4	4.737	B4	3.687	C4	3.960
5	A5	4.315	B5	4.234	C5	4.116
6	A6	4.713	B6	4.086	C6	4.421
7	A7	4.555	B7	3.215	C7	4.121
8	A8	3.958	B8	2.895	C8	2.916
9	A9	4.455	B9	3.125	C9	3.058
10	A10	4.618	B10	2.552	C10	3.896
11	A11	4.600	B11	2.430	C11	3.492
12	A12	4.239	B12	2.591	C12	3.969
13	A13	4.198	B13	2.965	C13	3.207
14	A14	3.861	B14	2.360	C14	3.918
15	A15	4.171	B15	2.191	C15	3.161
16	A16	4.271	B16	3.760	C16	3.343
17	A17	4.671	B17	3.511	C17	3.404
18	A18	4.558	B18	2.789	C18	3.570
19	A19	4.406	B19	2.504	C19	3.785
20	A20	4.141	B20	2.721	C20	3.402
21	A21	5.028	B21	3.017	C21	4.149
22	A22	5.009	B22	3.031	C22	4.165
23	A23	4.536	B23	2.852	C23	4.040
24	A24	5.106	B24	3.261	C24	3.741
25	A25	4.715	B25	3.149	C25	2.155

When analyzing the rank response of the RSW parameters, it was found that welding current had the greatest impact on the tensile shear force results, followed by pulse welding, holding time, welding time, squeezing time, and finally, pressure had the smallest impact on the 1–1 mm case. The impact of the RSW parameters on the tensile shear force of 1–1 mm case is summarized in the mean effect plots portrayed in Figure 9.

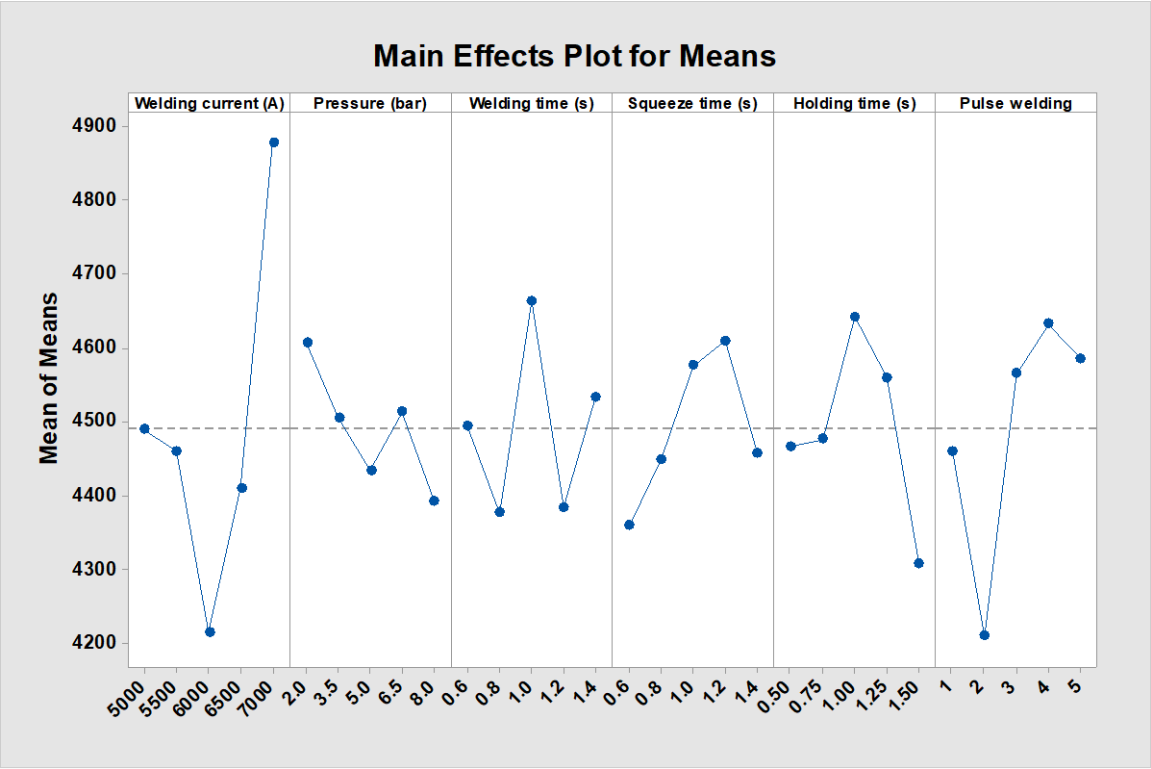

Figure 9. Shear force main effect plots of RSW parameters of 1–1 mm titanium alloy (case A).

The welding current being the greatest factor impacting the shear force results is attributed to the increased heat required to form a sufficient solid molten pool of weld at the interface of faying surfaces between the two titanium sheets. It is noteworthy that an improvement in shear force results was observed as the welding current was increased to 7000 A, reaching a maximum shear force of 4.879 kN. On the other hand, the minimal shear force was 4.214 kN, observed with a welding current of 6000 A.

When measuring the shear force effect caused by pulse welding, the minimum value was found to be attained with 2 pulses, while increasing the pulse welding increased shear force, with the maximum shear force being recorded at 4.632 kN with 4 pulses. The tensile shear force increased because the diameter of the nugget grew as the pulse welding was increased to 4 pulses [41]. Concerning the findings on holding time, it was seen that the tensile shear force exhibited a rise as the holding time was incrementally increased. This trend continued until a peak shear force of 4.632 kN was obtained, which occurred at a holding time of 1 s. Afterward, a rise in the duration of the holding time resulted in a reduction in the shear force. This is because the increase in holding time led to a reduction in the amount of the void that might be generated in the middle of the nugget region and, therefore, the shear force increased. Nevertheless, it is important to regulate the extent of this increase in hold time, as the researchers observed in the present investigation that a holding period beyond 1 s resulted in a decline in the tensile shear force. Following the prior study conducted by Long et al. [42], it is noteworthy that prolonging the holding period may significantly diminish the occurrence of voids in the RSW process.

Additionally, it has been confirmed the weld strength was compromised because of the existence of a void [43–46]. The increase of the welding time from 0.6 to 0.8 s results in a reduction in the tensile shear force from 4.494 to 4.376 kN. However, the further elevation in the welding time to 1 s caused the shear force to escalate, reaching its peak value of 4.664 kN. Increases in tensile shear force from 4.359 to 4.610 kN were seen when the squeeze time was increased from 0.6 to 1.2 s, but further increases in squeeze time resulted in decreased shear force.

Regarding the pressure impact on the shear force, it was revealed that the optimal tensile shear force was 4.607 kN with 2 bar as pressure; however, further raising the pressure from 3.5 to 5 bar, impacted the tensile shear force significantly and decreasing it to 4.434 kN. The tensile shear force of resistance spot welded joints reduced because the welding pressure was increased, resulting in a decrease in the amount of heat input, which is represented here as the welding current density passing through the nugget zone, resulting in an increase in the expulsion of the molten metal at the faying surfaces [19,47]. Another viewpoint holds that when welding pressure rises, a significant stress concentration is formed in the areas surrounding the weld nugget due to the indentions forced by the electrodes on the sheet. Lower tensile shear forces may be attributed to the use of greater welding pressures, which is caused by the production of a weak resistance spot welded connection that leads to the formation of brittle welds [48]. If the molten metal is expelled too forcefully from the nugget zone, it might cause a through-hole in the workpiece, which increases the risk of cracking and porosity developing in the weld itself [49].

Using the Taguchi method, it was determined that the RSW parameters of 5000 A welding current, 8 bar of pressure, 1.4 s each for welding and squeezing, 1.5 s for holding, and 5 pulses per weld produced the strongest resistance spot welded joints in case B with a tensile shear force of 4.234 kN. However, experiment 15 had the lowest tensile shear force at 2.191 kN with the following parameters: 6000 A welding current, 8 bar pressure, 0.8 s welding time, 1.2 s squeezing time, 0.5 s holding time, and 3 pulses per second of welding as depicted in Table 5. Unlike in case A, where welding current was the most influential factor, the welding time in case B was found to have the greatest impact on the tensile shear force when examining the main effects plot of case B on the tensile shear force regarding the rank effect of each RSW parameter of case B. As for the relative importance of the other factors in case B, the findings indicated that pulse welding was second, welding current was third, squeeze and holding times were rated fourth and fifth, and pressure was listed as the sixth and final response.

The main effects plot illustrating the means of case B concerning the welding current, as shown in Figure 10, revealed that the maximum tensile shear force was seen at a welding current of 5000 A, whilst the lowest value was recorded at 6000 A. The experimental findings about pressure welding indicate that the maximum tensile shear force was seen at a pressure of 2 bars, whilst the lowest value was observed at a pressure of 3.5 bar. The experimental results indicate that there is a significant relationship between welding duration and shear force. Specifically, as the welding time increased from 0.6 to 1.4 s, the shear force also increased, starting from its lowest value at 0.6 s and reaching its highest at 1.6 s.

Moreover, the results of the squeeze time experiment indicated a progressive rise in the tensile shear force until it reached its peak at 1 s. Subsequently, the shear force saw a decline and reached its minimal effect at 1.2 s. The results of the holding time experiment indicate that a duration of 1.25 s had the most significant impact, whereas a duration of 0.75 s had the least pronounced effect. The pulse welding process demonstrated the highest shear force when using 5 pulses, whereas the lowest shear force was seen when employing just 2 pulses.

Regarding the tensile shear force outcomes of the titanium alloy in case C, it was observed that the highest shear force value of 4.421 kN was obtained during experiment number 6. This experiment was conducted under the following welding conditions: a welding current of 5500 A, a pressure of 2 bar; and welding, squeeze, and holding times

of 0.8, 1, and 1.25 s, respectively. The pulse welding was of 5. On the other hand, the experimental analysis revealed that the minimum shear force, equivalent to 2.155 kN, was observed in experiment number 25 as shown in Table 5.

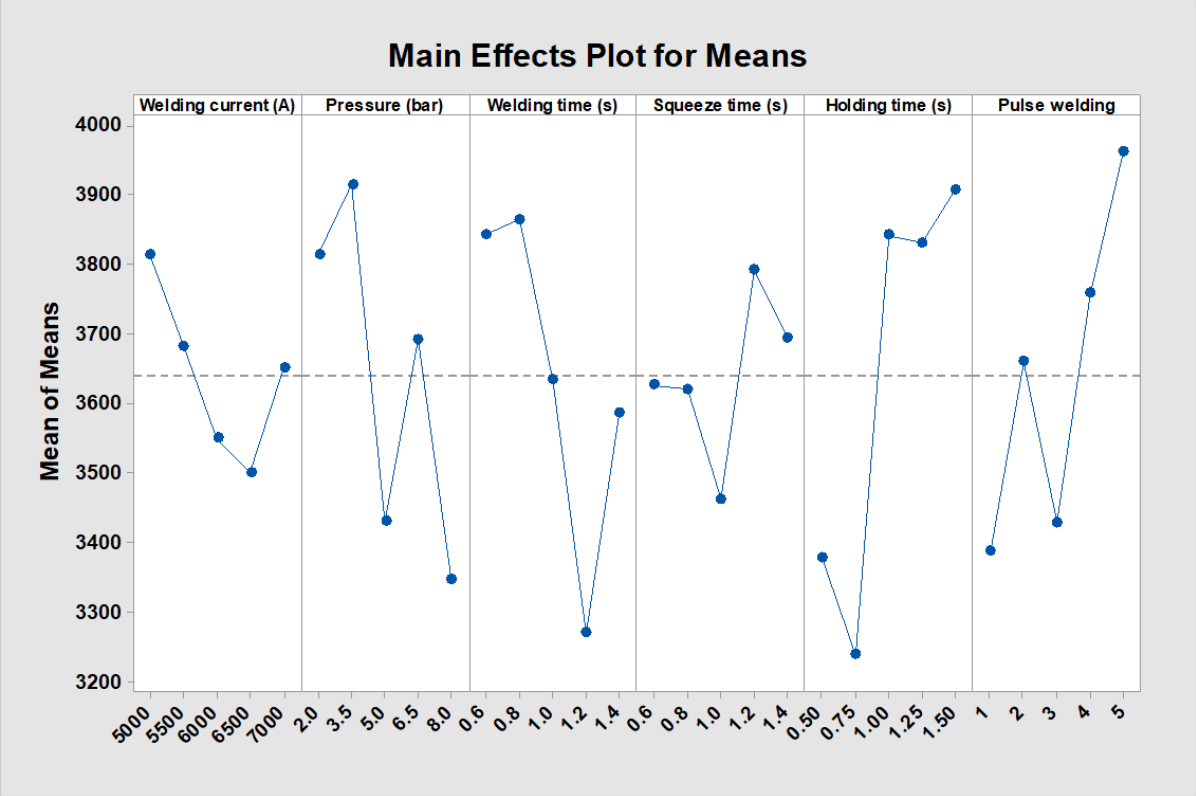

Figure 10. Shear force main effect plots of RSW parameters of 0.5–0.5 mm titanium alloy (case B).

The examination of the RSW rank response in case C showed that the holding time was the most significant factor, in contrast to cases A and B where the current and welding time had the most pronounced impact. The welding time exhibited the second-highest level of response, followed by pulse welding, which showed the third-highest level of influence. The squeeze time and pressure recorded the fourth and fifth highest impacts, respectively. In contrast, the welding current had the lowest effect, unlike in case A, where it had the highest impact.

The main effects graphs for the means of case C, as can be seen from Figure 11, indicate a progressive reduction in tensile shear force as the welding current increases, ranging from the highest value seen at 5000 A to the lowest shear force observed at 6500 A. The mean shear force was maximum at a pressure of 3.5 bar, while the lowest mean shear force was noted at a pressure of 8 bar. Regarding the welding time, the average shear force reached its peak at 0.8 s, while the lowest value was seen at 1.2 s. In contrast, for the squeeze time, the greatest mean shear force was recorded at 1.2 s, but the smallest mean shear force was observed at 1 s. The experimental results indicate that a holding time of 1.5 s provides the most favorable mean value, whilst the least desirable outcome emerged at a holding time of 0.75 s. As shown in the analysis of case B, it is evident that case C exhibited the highest mean shear force when subjected to a five-pulse welding process. Conversely, the lowest mean shear force for case C is observed when a one-pulse welding process was used.

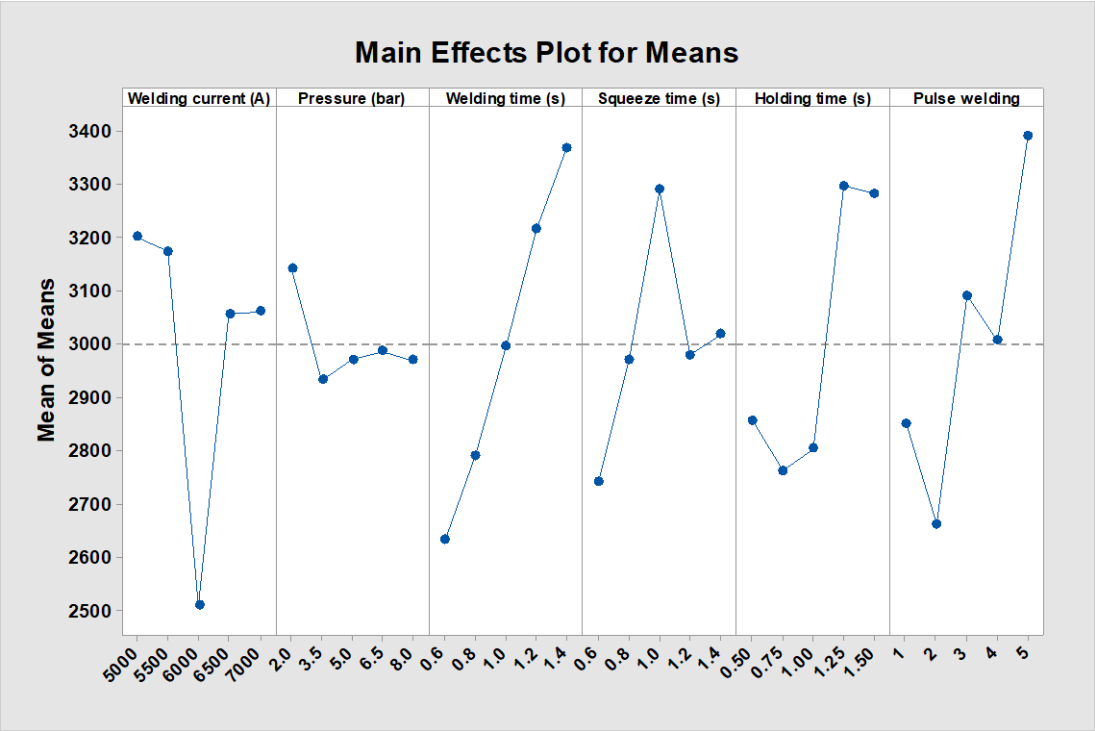

Figure 11. Shear force main effect plots of RSW parameters of 0.5–1 mm titanium alloy (case C).

4.2. Failure Mechanism

Resistance spot welded joints usually failed with the following failure modes: pull-out failure (PF) mode, interfacial mode (IF), partial interfacial mode (PIF), and partial pull-out through thickness (PPTT) mode [43,45,49–52]. The type of failure mode generated by resistance spot welded joints during a tensile shear test depends on the formed shape of the fusion zone (FZ), sheet metal thickness, heat-affected zone hardness, and weld nugget hardness [53].

Depending on the RSW settings and the sheet thickness of the welded joints, whether it was a similar or dissimilar thickness, different sorts of failure modes were identified. For case A, only sample 20A failed with interfacial failure mode as depicted in Figure 12. The shear force of this sample was 4.141 kN, while the other samples revealed pull-out failure (PF) with varying the location of failure initiation, whether it was around the nugget zone or heat-affected zone.

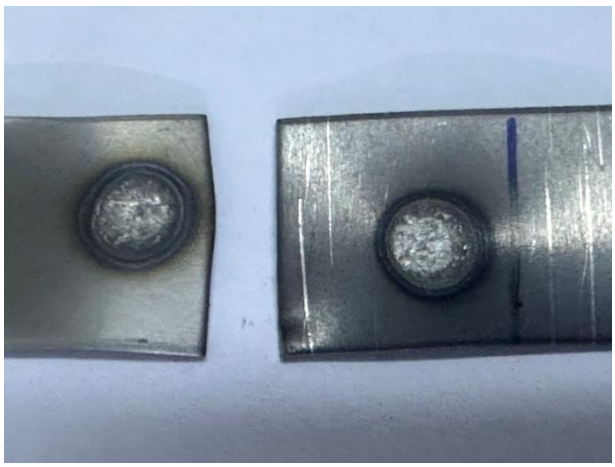

Figure 12. Interfacial failure of sample 20A.

Upon examination of the microstructure associated with interfacial failure, it was seen that voids and microcracks were present inside the nugget zone structure as shown in Figure 13a. Notably, the failure initiation was observed to occur near the fusion region as depicted in Figure 13b. The initiation of cracks occurred at the grain boundary, followed by their propagation over the grain boundary. This phenomenon is often referred to as trans-granular brittle fracture, which is recognized as the primary factor contributing to the reduction in tensile shear force. Pull-out failure mode was detected and initiated at the fusion area in the base metal for samples (1–3, 11, 16, 18, and 21–24)A. Tearing occurred as fractures propagated from the fusion site and completed across the breadth of the base metal. The highest tensile shear force (5.106 kN) was observed with this failure for sample 24A. Even though the same sort of failure was seen with sample 13A, the final failure was completed through the thickness of the base metal rather than the width. The failure of samples (4, 9, 10, and 14)A was due to pull-out around the HAZ region, where the lowest shear force was observed here with sample 14A. For the samples (5, 8, 12, 15, and 25)A, the pull-out failure type around the nugget zone was observed.

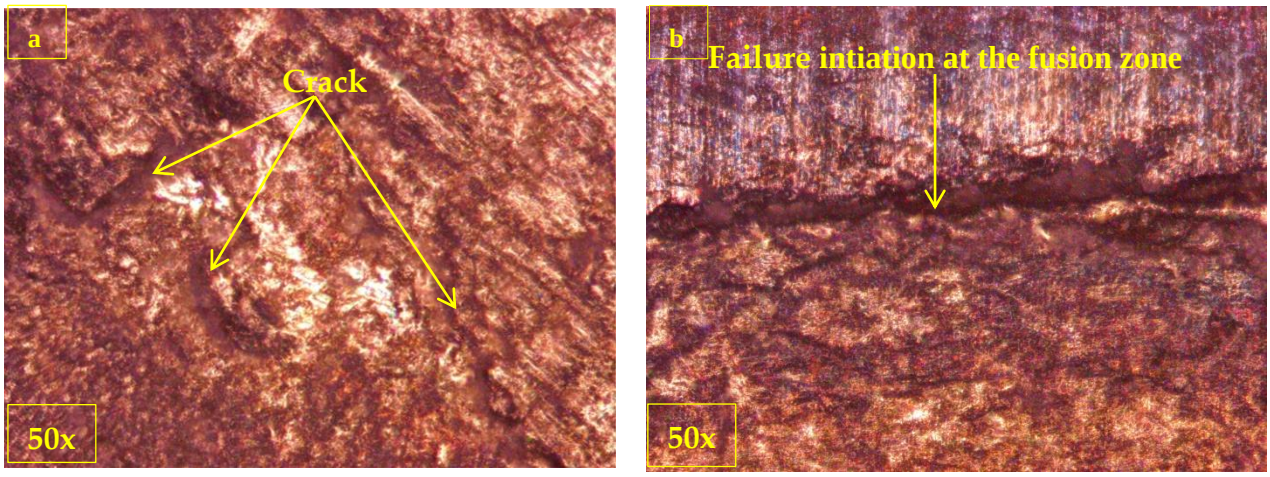

Figure 13. Micro-examination of the fractured surface of sample 20A at different sites, (**a**): cracks, (**b**): initiation of the crack.

In case B, it turned out that all 25 samples exhibited a full pull-out failure mechanism, as can be seen in Figure 14, irrespective of the RSW parameters used. However, it is worth noting that the specific site of failure within the welded joints varied. The pull-out failure mode appeared to start and end around the nugget for the samples marked as 1B, 2B, 9B, 12–14B, and 17–20B. Sample 5B had the maximum tensile shear force of 4.234 kN of the observed failure types.

The potential explanation for the failure seen in the nugget zone might be attributed to the weakening of this area. This weakening may be a result of the higher indentation depth induced by the higher heat created during the passage of greater electrical current through the welding electrodes. It is noteworthy to mention that the failure mode of pull-out for the designated samples 8B, 11B, and 15B began between the heat-affected zone and nugget zones. Specifically, pull-out started in the HAZ and then advanced towards the nugget region, ultimately resulting in fracture. This phenomenon could potentially be associated with the softening of the heat-affected zone, as shown by the findings from the tensile shear force test. Notably, the recorded minimum value of 2.191 kN further proves this claim. The initiation of the third case of the pull-out failure mechanism occurred in the HAZ and then, spread in the peripheral direction surrounding the HAZ until its completion.

Apart from sample number 8C, which exhibited a full interfacial failure mode as shown in Figure 15a, the resistance spot welded joints with an unequal thickness of 0.5 and 1 mm showed a pull-out failure mode. In contrast, samples numbers 13C and 15C failed with a partial failure between a large amount of interfacial failure and a small one of the

pull-out nugget mode, as shown in Figure 15b. As shown in Figure 16, the microscopic examination of the 8C cracked surface revealed the presence of a river-like pattern in the fractured spot area, which was created during the tensile shear test.

Figure 14. Pull-out nugget failure of case B.

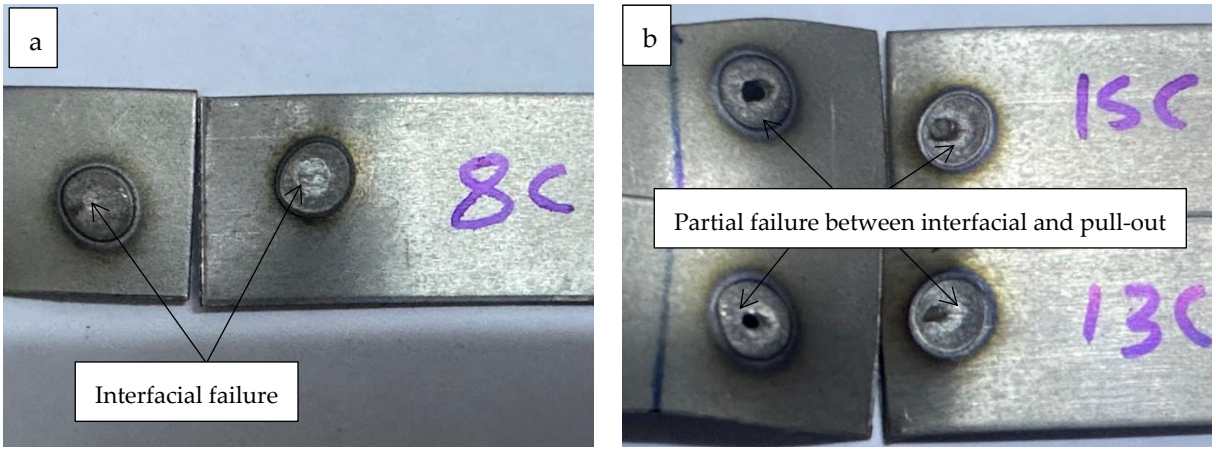

Figure 15. Failure mechanism of case C, (**a**): interfacial failure, (**b**): partial failure.

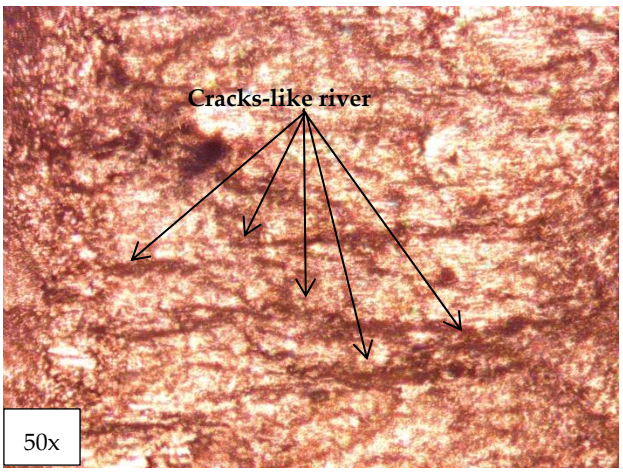

Figure 16. Micro-examination of the sample 8C.

This is because the orientations of each grain formed in the fusion area are different from one another, causing the crack division to occur in stages that resemble terraces. This kind of fracture is often known as a cleavage failure, and it is detrimental to the failure of the engineering component. However, the lowest tensile shear force was not shown in this sample. The visual observation of samples 13C and 15C, which failed with partial failure between pull-out nugget and interfacial modes, showed that the failure of these samples began as a brittle failure caused by the interfacial mode near the fusion region and progressed towards the nugget region.

The failure of the nugget zone originated as a brittle fracture and progressed to virtually the middle of the nugget zone before changing to a ductile fracture and leaving a small amount of nugget zone on the final surface of the fracture. The samples (7, 9, 14, 17, 16, and 20)C had a pull-out failure mode that began in the HAZ and ended in the same zone with a failure that resembled a cup and cone failure, indicating that the entire failure was ductile. In contrast, the subsequent specimens (1–6, 10–12, 19, 21–24)C failed using the same mechanism, but the failure began in the fusion boundary region.

The final specimen, 25C, had the maximum tensile shear force measured at 4.421 kN. This failure also happened in pull-out mode, first near the HAZ and then spreading out to the width where final tearing occurred. The most intriguing observation is related to the failure of resistance spot welded joints with unequal thicknesses. Regardless of the combination of the RSW parameters, it was observed that the nugget zone was extracted during the tensile shear test from the smaller 0.5 mm thickness towards the larger 1 mm thickness. This resulted in the final fractured surface of the 1 mm specimen resembling a conical nugget zone, while the 0.5 mm specimen exhibited a hole generated by the withdrawal of the nugget by the 1 mm sample.

4.3. Micro-Hardness Distribution

The hardness measurements were performed on three resistance spot welded samples of the three analyzed cases. These three samples were selected by the shear force measurements obtained by selecting the samples that exhibited the greatest, middle, and lowest shear force, respectively.

Since the base metal, heat-affected, welded nugget zones experienced different intensities of welding parameters in each sample, the microstructure of these three zones will be different and because of that, each zone will show a different micro-hardness value. Irrespective of each sample and case, the micro-hardness values were found to be greatest in the nugget zone and lowest in the base metal. The values in the heat-affected zone were about at the midpoint of those found in the other two regions.

Figure 17 shows the hardness distribution for case A. It can be observed that the Vickers hardness of the three samples rose gradually from the base metal zone to the heat-affected zone, reaching the nugget zone, and then reduced gradually again on the opposite side of the heat-affected zone and base metal. The highest micro-hardness of case A was observed with sample A14, which showed the lowest tensile shear force. A Vickers hardness of 184.3 HV was recorded for sample A14 at the nugget zone, whereas 153.3 HV was recorded for the heat-affected zone, while the base metal zone showed the lowest one of 137.7 HV.

As for sample number 24, which showed the highest tensile shear force, it was noted that this presented the lowest micro-hardness, where the hardness of the nugget zone reached 169.5 HV and 146.4 at HAZ, while the base metal recorded the minimum hardness of 135.8 HV. The micro-hardness measurements of sample A23 presented the same trend as the Vickers hardness noticed with samples A24 and A14, and the micro-hardness observations showed values between these samples. Moreover, the nugget zone of sample A23 showed the peak hardness, while the lowest hardness was noted with the base metal, and the HAZ presented values between the nugget and base metal zones.

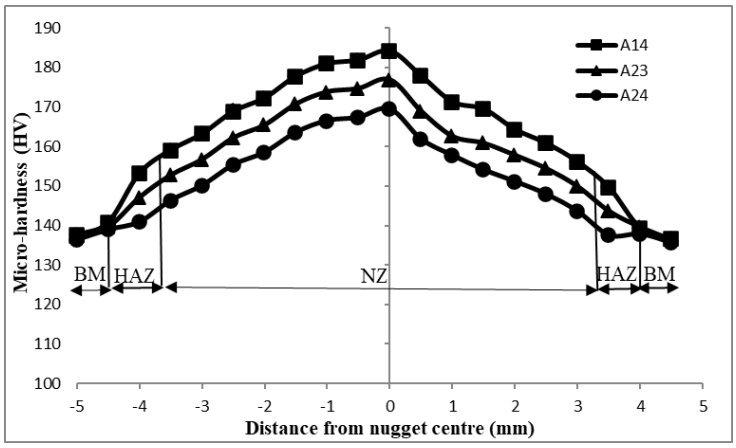

Figure 17. Micro-hardness results of 1–1 mm titanium alloy (case A).

When investigating the micro-hardness in case B, the Vickers hardness findings showed a noticeable enhancement in the hardness of the nugget zone compared to the base metal of the samples, while the heat-affected zone showed 187.8 HV. From the data shown in Figure 18, it can be inferred that the micro-hardness of sample B15 ranged from a high of 285 HV in the nugget zone to a low of 156.7 HV at the base metal.

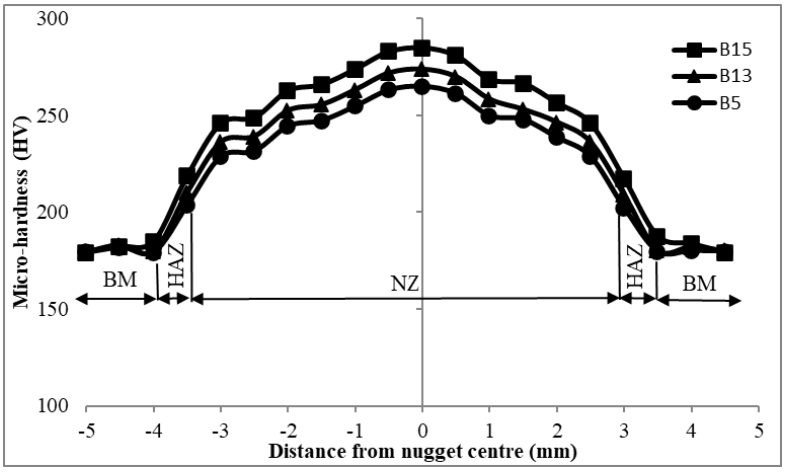

Figure 18. Micro-hardness results of 0.5–0.5 mm titanium alloy (case B).

It is worth noting that the samples of case B micro-hardness observations followed the same pattern as in case A. The highest micro-hardness was observed in the B15 sample, which exhibited the lowest tensile shear force. In addition, the lowest micro-hardness was noted in the B5 sample, which exhibited the highest tensile shear force, and the middle micro-hardness was observed in the B13 sample, which exhibited the middle shear force.

The micro-hardness results of titanium alloy in case C are displayed in Figure 19. The micro-hardness curve in case C showed a similar trend to cases A and B. The base metal showed the lowest hardness, and the nugget zone revealed its greatest hardness, followed by the HAZ micro-hardness. Sample C25, which had the minimum tensile shear force recorded, had the highest micro-hardness, as can be seen in Figure 19.

Vickers hardness measurements at the base metal of sample C25 showed that the lowest value was 134.5 HV. On the other hand, the greatest value was 220.4 HV in the nugget zone and 159.5 HV in the heat-affected zone. Similar to cases A and B, sample C6, which presented the maximum tensile shear force, showed the lowest micro-hardness at the nugget, HAZ, and base metal zones in comparison to samples C25 and C24.

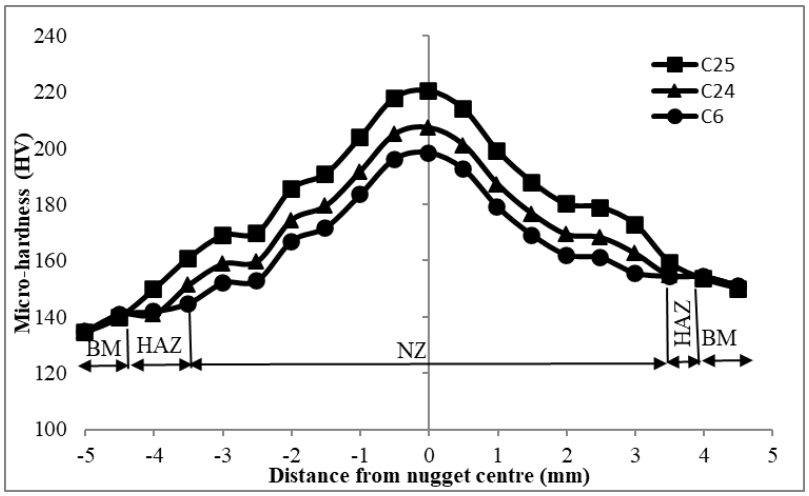

Figure 19. Micro-hardness results of 0.5–1 mm titanium alloy (case C).

This Vickers hardness improvement is due to the hard and brittle behavior of the resistance spot welded joint obtained. This means that an increase in the tensile shear force of the welded joints resulted in a decrease in micro-hardness as reported by Li et al. [22]. When attending to the welding parameters, the samples of case A were welded with the highest welding current of 6000 and 7000 A, while the samples of case B were welded with 5000 and 6000 A, respectively. The samples in case C were welded with welding currents of 5500 and 7000 A.

The variation in the welding current might be attributed to a change in the internal microstructure formation. For this reason, the welded samples are more likely to experience imperfections in the resultant spot welded joints through welding operations, as supported by Li et al. [22]. The reason for increasing the micro-hardness in the nugget zone compared to the heat-affected zone and base metal is due to the variation of alpha (α) and beta (β) phases in these regions. The formation of the α and β phases is dependent on the cooling rate; the RSW process is conducted at room temperature.

According to that, the cooling rate changes slowly from the center of the weld nugget zone, where the center of the heat input is located, to the heat-affected zone, which is located slightly away from the heat input source. Upon reaching the base metal, the nugget zone experiences a faster cooling rate compared to the other zones. Raising the cooling rate results in a smoother microstructure.

The faster cooling rate in the base metal causes the growth of α and β phase boundaries to be perpendicular to the lamellar and appear nucleated [6]. Because of that, the new lamellar structure does not form in the microstructure, particularly in the base metal. In addition, due to the thin size of the heat-affected zone, it will be able to accommodate the new lamellar structure owing to the reduced cooling rate. On the other hand, the weld nugget experiences a slower cooling rate as it is the main region of the heat input and has that slow cooling rate. This allows producing the new lamellar structure of the α and β phases. Therefore, increasing the hardness of the weld nugget zone, and the more lamellar structure that is formed, the more the hardness of the weld nugget increased [6].

4.4. Artificial Neural Network Prediction

Various neural network models have been developed to analyze the tensile shear force of the resistance spot welded joints of the three cases. Different transfer functions were trained with many training functions to determine the ideal neural network model by estimating the influence of the RSW parameters on the resultant shear force of welded joints. Mean squared error (MSE) and coefficient of determination (R^2) were used as validation metrics for comparing the actual results with the predicted ones. Table 6 lists the MSE and R^2 results with the different training and transfer functions.

Table 6. MSE and R^2 for different training and transfer functions.

Training Function	Transfer Function	MSE	R^2
Trainlm	Logsig	0.01821	0.98433
	Tansig	0.04151	0.96390
	Purelin	0.10719	0.90377
Traincgp	Logsig	0.03533	0.97006
	Tansig	0.05336	0.95587
	Purelin	0.11669	0.89503
Trainscg	Logsig	0.04449	0.96146
	Tansig	0.08234	0.92700
	Purelin	0.10950	0.90158
Traincgf	Logsig	0.04450	0.96200
	Tansig	0.06238	0.94526
	Purelin	0.11491	0.90088
Traincgb	Logsig	0.04810	0.95941
	Tansig	0.06574	0.94382
	Purelin	0.12269	0.89377

It can be noted from the data in Table 6 that the Levenberg–Marquardt (Trainlm) training function with the log sigmoid transfer function (Logsig) achieved the best results for the validation metrics MSE and R^2. From the findings shown in Table 6 and Figure 20, it is obvious that the maximum prediction was obtained when employing the Levenberg–Marquardt (Trainlm) training function with the log sigmoid transfer function (Logsig), where the MSE and R^2 were 0.01821 and 0.98433, respectively. Furthermore, the lowest prediction with the Trainlm training function was achieved when pure linear (Purelin) was applied; the MSE and R^2 were recorded to be 0.10719 and 0.90377, respectively.

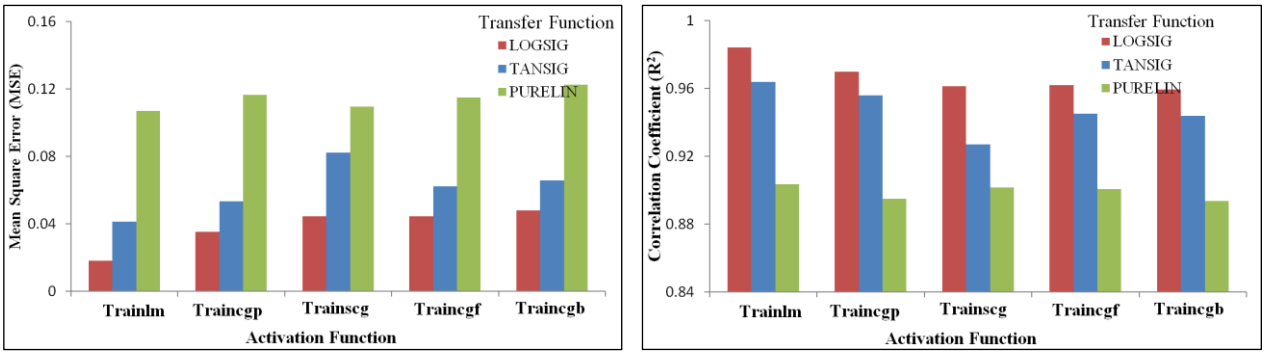

Figure 20. MSE and R^2 for predicted results with various training and transfer functions.

The Tansig transfer function with the Trainlm training function presented modest results and was better than the Purelin transfer function, where the MSE and R^2 were determined to be 0.04151 and 0.96390, respectively. On the other hand, the conjugate gradient with Powell–Beale restarts (Traincgb) training function recorded the worst prediction with all transfer functions compared to the other training functions used in the neural network models. The MSE and R^2 were 0.04810 and 0.95941, respectively, when the Traincgb training function was trained with the Logsig transfer function, while the Purelin transfer function with the Traincgb training function presented the worst prediction, with the MSE and R^2 recorded to be 0.12269 and 0.89377, respectively. Table 7 shows the predicted and actual tensile shear force of the A, B, and C cases with the optimal neural network model using the Trainlm training function with the Logsig transfer function.

Table 7. Actual and predicted shear force using the optimal NN model (Trainlm with Logsig).

Sample No.	Welding Cases								
	A			B			C		
	Actual (kN)	Predicted (kN)	Error %	Actual (kN)	Predicted (kN)	Error %	Actual (kN)	Predicted (kN)	Error %
1	4.423	3.973	10.174	2.422	2.228	8.010	3.665	4.162	11.941
2	4.052	4.2017	3.677	2.317	2.339	0.950	3.916	4.125	5.067
3	4.918	4.836	1.647	3.352	3.249	3.073	3.412	3.601	5.221
4	4.737	4.806	1.436	3.687	3.750	1.709	3.960	3.989	0.702
5	4.315	4.322	0.162	4.234	4.187	1.110	4.116	4.126	0.218
6	4.713	4.599	2.419	4.086	3.857	5.580	4.421	4.292	3.006
7	4.555	4.698	3.117	3.215	3.404	5.879	4.121	4.064	1.403
8	3.958	3.918	0.985	2.895	2.465	14.853	2.916	2.779	4.894
9	4.455	4.322	2.963	3.125	3.002	3.936	3.058	3.071	0.391
10	4.618	4.577	0.866	2.552	2.550	0.039	3.896	3.969	1.839
11	4.600	4.644	0.935	2.430	2.547	4.774	3.492	3.591	2.757
12	4.239	4.307	1.604	2.591	2.638	1.775	3.969	3.945	0.583
13	4.198	4.118	1.882	2.965	2.868	3.238	3.207	3.117	2.855
14	3.861	3.988	3.289	2.360	2.444	3.559	3.918	3.901	0.436
15	4.171	4.139	0.743	2.191	2.228	1.643	3.161	3.167	0.158
16	4.271	4.370	2.318	3.760	3.764	0.106	3.343	3.432	2.593
17	4.671	4.658	0.257	3.511	3.512	0.028	3.404	3.375	0.830
18	4.558	4.609	1.119	2.789	2.785	0.108	3.570	3.546	0.649
19	4.406	4.451	0.999	2.504	2.466	1.478	3.785	3.756	0.772
20	4.141	4.129	0.266	2.721	2.902	6.652	3.402	3.547	4.060
21	5.028	4.999	0.557	3.017	3.117	3.281	4.149	4.123	0.606
22	5.009	4.938	1.397	3.031	3.023	0.231	4.165	4.169	0.072
23	4.536	4.524	0.243	2.852	2.888	1.262	4.040	3.989	1.253
24	5.106	5.083	0.450	3.261	3.277	0.491	3.741	3.739	0.053
25	4.715	4.703	0.233	3.149	3.095	1.683	2.155	2.571	16.180

It is worth mentioning that the Logsig transfer function gives the best prediction with the different training functions, while the Purelin transfer function revealed the worst prediction with the same training function. Moreover, the second highest estimation was achieved by adopting the conjugate gradient with Polak–Ribiére updates (Traincgp) training function with Logsig transfer function, where the MSE and R^2 values were 0.03533 and 0.97006, respectively.

Despite the Traincgp training function with Logsig transfer function, which presented the second highest prediction, the Purelin transfer function was given the second lowest prediction compared to the other models by determining the MSE and R^2 of 0.11669 and 0.89503, respectively. Moreover, the MSE and R^2 results from using the Trainscg training function with the Logsig transfer function were 0.04449 and 0.96146, respectively. Again, the MSE and R^2 decreased to 0.10950 and 0.90158 when adopting the Trainscg training function with the Purelin transfer function.

For a conjugate gradient with Fletcher–Reeves updates (Traincgf) training function, the Logsig transfer function gives values of MSE and R^2 equal 0.04450 and 0.96200, respectively. The Purelin transfer function with the Traincgf training function recorded the MSE and R^2 of 0.11491 and 0.89377, respectively. Figures 21 and 22 show the best performance and actual and predicted data curves of the optimal model when using the Trainlm training function with the Logsig transfer function.

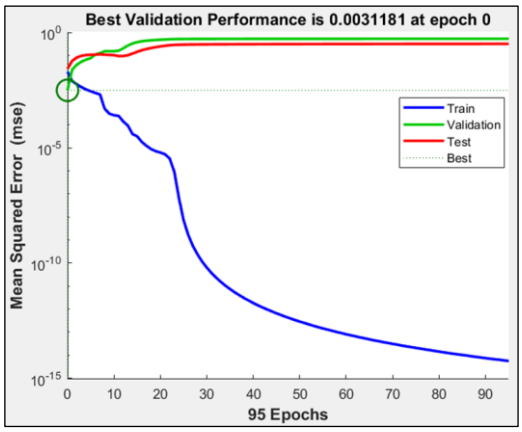

Figure 21. Performance curve of neural network model of shear force using Trainlm with Logsig.

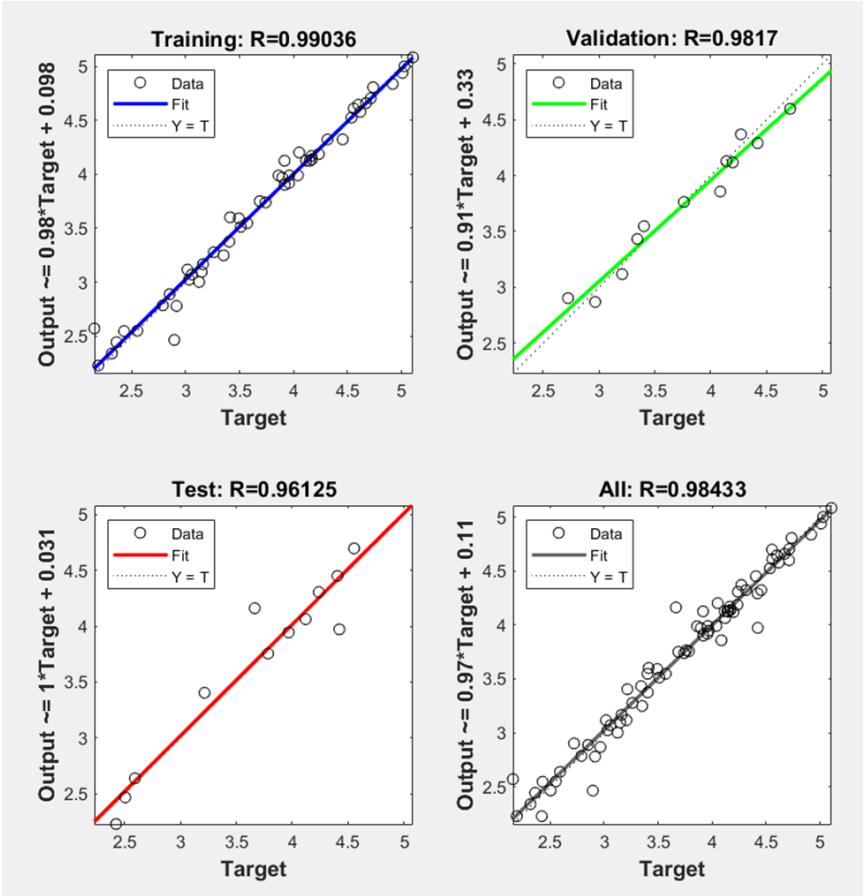

Figure 22. Regression curve of actual and predicted data of shear force using Trainlm with Logsig.

5. Conclusions

In the present work, we investigated the impact of RSW parameters like welding current, pressure, welding time, squeeze time, holding time, and pulse welding on the tensile shear force, failure mechanism, and micro-hardness of welded joints made from titanium alloy of thickness 1 and 0.5 mm with different combinations of equal and unequal thickness. Moreover, an artificial neural network model was applied to predict the impact of the RSW process parameters on the tensile shear force. The following remarks can be drawn:

- Case A presented the highest tensile shear observations, while case C gave the second maximum tensile shear force. The lowest tensile shear force observations were noticed in case B.
- The maximum hardness was observed with a minimum tensile shear force sample, while the lowest hardness was recorded with the highest tensile shear force sample. Furthermore, the nugget zone presented the maximum hardness, followed by the HAZ, while the lowest hardness was noted at the base metal zone.
- The maximum micro-hardness was attained in case B. The second highest hardness measurements were determined to be with case C, and case A showed the minimum hardness.
- Pull-out nugget failure type was observed with all samples of case A, except one sample that failed with an interfacial mode. The failure mechanism of the case B samples was a pull-out nugget failure varying the failure location (around the nugget zone or the HAZ). Most of the case C samples failed with pull-out nugget type except one sample that failed with full interfacial mode. Some samples of case C showed partial failure between the pull-out and interfacial failure.
- Artificial neural network models presented a significant finding in predicting the actual data and minimizing the error in the RSW process.
- The most interesting observation about the neural network model is that the Trainlm training function gives the best performance when using the Logsig as a transfer function. The Trainlm training function with Logsig transfer function gives the best performance in predicting tensile shear force where the MSE and R^2 were 0.01821 and 0.98433, respectively. The Purelin transfer function revealed a lower MSE and R^2 of 0.10719 and 0.90377, respectively, when trained with Trainlm function.
- The lowest prediction of tensile shear force was achieved with Traincgb training function by adopting the Purelin transfer function with an MSE and R^2 of 0.12269 and 0.89377, respectively. The Logsig transfer function gave a higher MSE and R^2 of 0.0481 and 0.95941 when trained with the Traincgb function, but this was still lower than the validation metrics compared to the other training functions.

6. Recommendation for Future Work

Moving forward, there is some pending research that would help improve the understanding of the RSW process, particularly for titanium alloys. In this sense, it is suggested to carry out the following activities:

- To study the effect of the RSW parameters on the joint quality of other thicknesses.
- To analyze in detail the microstructure of the welded joints using X-ray diffraction (XRD), scanning electron microscopy (SEM), or tunneling electron microscope (TEM) techniques.

Author Contributions: Conceptualization, M.T.M. and A.P.; methodology, M.T.M. and A.P.; software, M.T.M.; validation, M.T.M., D.C. and A.P.; formal analysis, M.T.M., D.C. and A.P.; investigation, M.T.M. and A.P.; resources, M.T.M., D.C. and A.P.; data curation, M.T.M., D.C. and A.P.; writing—original draft preparation, M.T.M.; writing—review and editing, M.T.M., D.C. and A.P.; visualization, A.P.; supervision, A.P.; project administration, A.P.; funding acquisition, M.T.M., D.C. and A.P. All authors have read and agreed to the published version of the manuscript.

Funding: This research received no external funding.

Data Availability Statement: The raw data supporting the conclusions of this article will be made available by the authors on request.

Acknowledgments: The research reported in this paper was supported by the University of Vigo, Doctoral Program: Aerospace Technology: Electromagnetic, Electronic, Computer, and Mechanical Engineering.

Conflicts of Interest: The authors declare no conflicts of interest.

References

1. Pal, T.; Chattopadhyay, K. Resistance spot weldability and high cycle fatigue behaviour of martensitic (M190) steel sheet. *Fatigue Fract. Eng. Mater. Struct.* **2010**, *34*, 46–52. [CrossRef]
2. Banerjee, P.; Sarkar, R.; Pal, T.; Shome, M. Effect of nugget size and notch geometry on the high cycle fatigue performance of resistance spot welded DP590 steel sheets. *J. Mater. Process. Technol.* **2016**, *238*, 226–243. [CrossRef]
3. He, Y.; Yang, K.; Wang, X.; Huang, H.; Chen, J. Quality prediction and parameter optimisation of resistance spot welding using machine learning. *Appl. Sci.* **2022**, *12*, 9625. [CrossRef]
4. Lin, P.C.; Pan, J.; Pan, T. Failure modes and fatigue life estimations of spot friction welds in lap-shear specimens of aluminum 6111-T4 sheets. Part 2: Welds made by a flat tool. *Int. J. Fatigue* **2008**, *30*, 90–105. [CrossRef]
5. Peterson, W.; Borchelt, J. Maximizing cross tension impact properties of spot welds in 1.5 mm low carbon, dual-phase, and martensitic steels. In *International Body Engineering Conference & Exposition*; SAE International: Warrendale, PA, USA, 2000. [CrossRef]
6. Fatmahardi, I.; Mustapha, M.; Ahmad, A.; Ginta, T.L.; Taufiqurrahman, I.; Danish, M. Effect of welding parameters on the properties of the Ti-6Al-4V plate resistance spot weld joint. In *IOP Conference Series: Materials Science and Engineering*; IOP Publishing: Bristol, UK, 2021; Volume 1101, p. 012036. [CrossRef]
7. Das, T.; Rawal, S.; Panda, S.K.; Paul, J. Resistance spot-welding of AISI-1008 steel joints with MWCNT coating interlayer. *Mater. Manuf. Process.* **2020**, *36*, 448–456. [CrossRef]
8. Zhao, D.; Ren, D.; Song, G.; Zhao, K.; Zhang, Z. Nugget formation analysis of Al/Steel clinch resistance hybrid spot welding. *Sci. Technol. Weld. Join.* **2021**, *26*, 439–447. [CrossRef]
9. Deng, L.; Li, Y.; Cai, W.; Haselhuhn, A.; Carlson, B. Simulating Thermoelectric Effect and Its Impact on Asymmetric Weld Nugget Growth in Aluminum Resistance Spot Welding. *J. Manuf. Sci. Eng.* **2020**, *142*, 091001. [CrossRef]
10. Atasoy, E.; Kahraman, N. Diffusion bonding of commercially pure titanium to low carbon steel using a silver interlayer. *Mater. Charact.* **2006**, *59*, 1481–1490. [CrossRef]
11. Cui, C.; Hu, B.; Zhao, L.; Liu, S. Titanium alloy production technology, market prospects and industry development. *Mater. Des.* **2011**, *32*, 1684–1691. [CrossRef]
12. Sun, Z.; Pan, D.; Zhang, W. Correlation between welding parameters and microstructures in TIG, plasma and laser welded Ti-6Al-4V. In Proceedings of the 6th International Conference Trends in Welding Research, Pine Mountain, GA, USA, 15–19 April 2002; pp. 760–767.
13. Blackburn, J. Laser welding of metals for aerospace and other applications. *Weld. Join. Aerosp. Mater.* **2012**, 75–108. [CrossRef]
14. Freeman, R. New welding techniques for aerospace engineering. *Weld. Join. Aerosp. Mater.* **2012**, 3–24. [CrossRef]
15. Liu, H.; Nakata, K.; Yamamoto, N.; Liao, J. Microstructural characteristics and mechanical properties in laser beam welds of Ti6Al4V alloy. *J. Mater. Sci.* **2012**, *47*, 1460–1470. [CrossRef]
16. Zhang, Y.; Sato, Y.S.; Kokawa, H.; Seung Park, S.H.C.; Hirano, S. Microstructural characteristics and mechanical properties of Ti–6Al–4V friction stir welds. *Mater. Sci. Eng. A* **2008**, *485*, 448–455. [CrossRef]
17. Mironov, S.; Zhang, Y.; Sato, Y.S.; Kokawa, H. Development of grain structure in β-phase field during friction stir welding of Ti–6Al–4V alloy. *Scr. Mater.* **2008**, *59*, 27–30. [CrossRef]
18. Buffa, G.; Ducato, A.; Fratini, L. FEM based prediction of phase transformations during friction stir welding of Ti6Al4V titanium alloy. *Mater. Sci. Eng. A* **2013**, *581*, 56–65. [CrossRef]
19. Zhang, X.; Zhang, J.; Fei Chen, F.; Yang, Z.; He, J. Characteristics of Resistance Spot Welded Ti6Al4V Titanium Alloy Sheets. *Metals* **2017**, *7*, 424. [CrossRef]
20. El Kandaoui, M.; Scandella, F.; Germain, L.; Brandy, P.; Debreyer, D.; Gérardin, C.; Fleury, É. Microstructure and Mechanical Properties of Ti-6Al-4V Laser Welds for Airplane Floor Manufacturing Application. In *Proceedings of the 13th World Conference on Titanium*; John Wiley & Sons, Inc.: Hoboken, NJ, USA, 2016; pp. 1551–1556. [CrossRef]
21. Chen, S.; Sun, T.; Jiang, X.; Qi, J.; Zeng, R. Online monitoring and evaluation of the weld quality of resistance spot welded titanium alloy. *J. Manuf. Process.* **2016**, *23*, 183–191. [CrossRef]
22. Mansor, M.S.M.; Yusof, F.; Ariga, T.; Miyashita, Y. Microstructure and mechanical properties of micro-resistance spot welding between stainless steel 316L and Ti-6Al-4V. *Int. J. Adv. Manuf. Technol.* **2018**, *96*, 2567–2581. [CrossRef]
23. Li, Y.; Zhang, Y.; Luo, Z. Microstructure and mechanical properties of Al/Ti joints welded by resistance spot welding. *Sci. Technol. Weld. Join.* **2015**, *20*, 385–394. [CrossRef]
24. Lacki, P.; Niemiro, J. Strength evaluation of the beam made of the titanium sheets Grade 2 and Grade 5 welded by Resistance Spot Welding. *Compos. Struct.* **2017**, *159*, 538–547. [CrossRef]
25. Anna, D.; Marcin, D.; Piotr, L. Evaluation of load-bearing capacity of resistance spot welding (RSW) joints made of titanium Gr 5 sheets. *Key Eng. Mater.* **2016**, *687*, 212–219. [CrossRef]
26. Arunchai, T.; Sonthipermpoon, K.; Apichayakul, P.; Tamee, K. Resistance Spot Welding Optimization Based on Artificial Neural Network. *Int. J. Manuf. Eng.* **2014**, *2014*, 154784. [CrossRef]
27. Wan, X.; Wang, Y.; Zhao, D.; Huang, Y. A comparison of two types of neural network for weld quality prediction in small scale resistance spot welding. *Mech. Syst. Signal Process.* **2017**, *93*, 634–644. [CrossRef]
28. Ghafarallahi, E.; Farrahi, G.H.; Amiri, N. Acoustic simulation of ultrasonic testing and neural network used for diameter prediction of three-sheet spot welded joints. *J. Manuf. Process.* **2021**, *64*, 1507–1516. [CrossRef]

29. Bi, Y.; Yang, Y.; Luo, Z. Evolution mechanism of fracture interface wave and microstructure during resistance butt spot welding. *J. Manuf. Process.* **2023**, *101*, 1101–1108. [CrossRef]
30. Piotr, L.; Judyta, N. Numerical and experimental analysis of lap joints made of grade 2 titanium and grade 5 titanium alloy by resistance spot welding. *Materials* **2023**, *16*, 2038. [CrossRef] [PubMed]
31. Yu, J.; Zhang, H.; Wang, B.; Du, R.; Fan, Y.; He, P. Interfacial evolution behavior and mechanical properties of Ti/steel joint via ultrasonic seam assisted resistance spot welding with Cu interlayer. *J. Manuf. Process.* **2023**, *95*, 535–550. [CrossRef]
32. Santhakumari, A.; Senthilkumar, T.; Mahadevan, G.; Ramasamy, N. Interface and microstructural characteristics of titanium and 304 stainless steel dissimilar joints by upset butt welding using a gleeble thermo mechanical simulator. *J. Mater. Res. Technol.* **2023**, *26*, 7460–7470. [CrossRef]
33. Butsykin, S.; Slobodyan, M.; Strelkova, I.; Klimenov, V.; Elkin, M.; Gordynets, A.; Kiselev, A. Effects of preheating and slow cooling stages in small-scale resistance spot welding of the Ti-2Al-1Mn alloy. *Int. J. Adv. Manuf. Technol.* **2023**, *128*, 3011–3024. [CrossRef]
34. Niu, S.; Wang, Z.; Lou, M.; Ma, Y.; Lei, H.; Li, Y. Resistance rivet welding of aluminum/titanium dissimilar materials. *J. Manuf. Process.* **2023**, *108*, 141–152. [CrossRef]
35. Bi, Y.; Xu, Y.; Luo, Z. Material characterization and mechanical performance of laser diffusion welded joint between titanium alloy and stainless steel. *Mater. Lett.* **2023**, *336*, 133927. [CrossRef]
36. Liu, F.; Chen, Y.; Li, L.; Wang, C.; Wang, Q.; Liu, Y. Influence of welded pores on fatigue behavior of TC17 titanium alloy welded joints subjected to gigacycle regime at room and high temperatures. *J. Mater. Sci. Technol.* **2024**, *178*, 1–21. [CrossRef]
37. Mezher, M.T.; Saad, M.L.; Barrak, O.S.; Hussein, S.K.; Shakir, R.A. Multi-coupled field simulation and experimental study of AISI 316L stainless steel using resistance spot welding. *J. Mech. Eng. Res. Dev.* **2021**, *44*, 150–160.
38. *ANSI/AWS C1.1M/C1.1*; Recommended Practices for Resistance Welding. American Welding Society: Doral, NW, USA, 2012.
39. Beale, M.H.; Hagan, M.T.; Demuth, H.B. *Neural Network ToolboxTM User's Guide R2013b*; Mathworks Inc.: Natick, MA, USA, 2013.
40. Chakraborty, A.; Roy, S.; Banerjee, R. An experimental based ANN approach in mapping performance- emission characteristics of a diesel engine operating in dual-fuel mode with LPG. *J. Nat. Gas Sci. Eng.* **2015**, *28*, 15–30. [CrossRef]
41. Kaya, Y.; Kahraman, N. The effects of electrode force, welding current and welding time on the resistance spot weldability of pure titanium. *Int. J. Adv. Manuf. Technol.* **2012**, *60*, 127–134. [CrossRef]
42. Long, H.; Hu, Y.; Jin, X.; Shao, J.; Zhu, H. Effect of holding time on microstructure and mechanical properties of resistance spot welds between low carbon steel and advanced high strength steel. *Comput. Mater. Sci.* **2016**, *117*, 556–563. [CrossRef]
43. Paventhan, R.; Lakshminarayanan, P.R.; Balasubramanian, V. Prediction and optimization of friction welding parameters for joining aluminium alloy and stainless steel. *Trans. Nonferrous Met. Soc. China* **2011**, *21*, 1480–1485. [CrossRef]
44. Pouranvari, M.; Marashi, S.P.H. Failure mode transition in AHSS resistance spot welds. Part I. Controlling factors. *Mater. Sci. Eng. A* **2011**, *528*, 8337–8343. [CrossRef]
45. Pouranvari, M.; Marashi, S.P.H. Failure of resistance spot welds: Tensile shear versus coach peel loading conditions. *Ironmak. Steelmak. Process. Prod. Appl.* **2012**, *39*, 104–111. [CrossRef]
46. Pouranvari, M.; Marashi, S.P.H. Critical review of automotive steels spot welding: Process, structure and properties. *Sci. Technol. Weld. Join.* **2013**, *18*, 361–403. [CrossRef]
47. Zeytin, H.K.; Emre, H.E.; Kaçar, R. Properties of resistance spotwelded TWIP steels. *Metals* **2017**, *7*, 14. [CrossRef]
48. Fan, Q.; Xu, G.; Gu, X. Expulsion characterization of stainless steel resistance spot welding based on dynamic resistance signal. *J. Mater. Process. Technol.* **2016**, *236*, 235–240. [CrossRef]
49. Ma, C.; Chen, D.L.; Bhole, S.D.; Boudreau, G.; Lee, A.; Biro, E. Microstructure and fracture characteristics of spot-welded DP600 steel. *Mater. Sci. Eng. A* **2008**, *485*, 334–346. [CrossRef]
50. Alizadeh-Sh, M.; Marashi, S.P.H.; Pouranvari, M. Resistance spot welding of AISI 430 ferritic stainless steel: Phase transformations and mechanical properties. *Mater. Des.* **2014**, *56*, 258–263. [CrossRef]
51. Bouyousfi, B.; Sahraoui, T.; Guessasma, S.; Chaouch, K.T. Effect of process parameters on the physical characteristics of spot weld joints. *Mater. Des.* **2007**, *28*, 414–419. [CrossRef]
52. Pouranvari, M.; Marashi, S.P.H.; Safanama, D.S. Failure mode transition in AHSS resistance spot welds. Part II: Experimental investigation and model validation. *Mater. Sci. Eng. A* **2011**, *528*, 8344–8352. [CrossRef]
53. Marashi, P.; Pouranvari, M.; Amirabdollahian, S.; Abedi, A.; Goodarzi, M. Microstructure and failure behavior of dissimilar resistance spot welds between low carbon galvanized and austenitic stainless steels. *Mater. Sci. Eng. A* **2008**, *480*, 175–180. [CrossRef]